RESEARCH ARTICLE

Impact of Tissue Classification in MRI-Guided Attenuation Correction on Whole-Body Patlak PET/MRI

Mingzan Zhuang,[1,2] Nicolas A. Karakatsanis,[3] Rudi A. J. O. Dierckx,[1] Habib Zaidi [1,4,5,6]

[1]*Department of Nuclear Medicine and Molecular Imaging, University of Groningen, University Medical Center, 9700 RB, Groningen, The Netherlands*

[2]*Department of Radiation Oncology, Affiliated Hospital of Yangzhou University, Yangzhou, 225012, Jiangsu, China*

[3]*Division of Radiopharmaceutical Sciences, Department of Radiology, Weill Cornell Medical College, Cornell University, New York, NY, 10021, USA*

[4]*Division of Nuclear Medicine and Molecular Imaging, Geneva University Hospital, 1211, Geneva, Switzerland*

[5]*Geneva University Neurocenter, University of Geneva, 1205, Geneva, Switzerland*

[6]*Department of Nuclear Medicine, University of Southern Denmark, 500, Odense, Denmark*

Abstract

Purpose: The aim of this work is to investigate the impact of tissue classification in magnetic resonance imaging (MRI)-guided positron emission tomography (PET) attenuation correction (AC) for whole-body (WB) Patlak net uptake rate constant (K_i) imaging in PET/MRI studies. *Procedures:* WB dynamic PET/CT data were acquired for 14 patients. The CT images were utilized to generate attenuation maps (μ-map$_{CTAC}$) of continuous attenuation coefficient values (A_{coeff}). The μ-map$_{CTAC}$ were then segmented into four tissue classes (μ-map$_{4\text{-classes}}$), namely background (air), lung, fat, and soft tissue, where a predefined A_{coeff} was assigned to each class. To assess the impact of bone for AC, the bones in the μ-map$_{CTAC}$ were then assigned a predefined soft tissue A_{coeff} (0.1 cm^{-1}) to produce an AC μ-map without bones (μ-map$_{no\text{-bones}}$). Thereafter, both WB static SUV and dynamic PET images were reconstructed using μ-map$_{CTAC}$, μ-map$_{4\text{-classes}}$, and μ-map$_{no\text{-bones}}$ (PET$_{CTAC}$, PET$_{4\text{-classes}}$, and PET$_{no\text{-bones}}$), respectively. WB indirect and direct parametric K_i images were generated using Patlak graphical analysis. Malignant lesions were delineated on PET images with an automatic segmentation method that uses an active contour model (MASAC). Then, the quantitative metrics of the metabolically active tumor volume (MATV), target-to-background (TBR), contrast-to-noise ratio (CNR), peak region-of-interest (ROI$_{peak}$), maximum region-of-interest (ROI$_{max}$), mean region-of-interest (ROI$_{mean}$), and metabolic volume product (MVP) were analyzed. The Wilcoxon test was conducted to assess the difference between PET$_{4\text{-classes}}$ and PET$_{no\text{-bones}}$ against PET$_{CTAC}$ for all images. The same test was also adopted to compare the differences between SUV, indirect K_i, and direct K_i images for each evaluated AC method.

Correspondence to: Habib Zaidi; e-mail: habib.zaidi@hcuge.ch

Results: No significant differences in MATV, TBR, and CNR were observed between $PET_{4\text{-}classes}$ and PET_{CTAC} for either SUV or K_i images. $PET_{4\text{-}classes}$ significantly overestimated ROI_{peak}, ROI_{max}, ROI_{mean}, as well as MVP scores compared with PET_{CTAC} in both SUV and K_i images. SUV images exhibited the highest median relative errors for $PET_{4\text{-}classes}$ with respect to PET_{CTAC} ($RE_{4\text{-}classes}$): 6.91 %, 6.55 %, 5.90 %, and 6.56 % for ROI_{peak}, ROI_{max}, ROI_{mean}, and MVP, respectively. On the contrary, K_i images showed slightly reduced $RE_{4\text{-}classes}$ (indirect 5.52 %, 5.95 %, 4.43 %, and 5.70 %, direct 6.61 %, 6.33 %, 5.53 %, and 4.96 %) for ROI_{peak}, ROI_{max}, ROI_{mean}, and MVP, respectively. A higher TBR was observed on indirect and direct K_i images relative to SUV, while direct K_i images demonstrated the highest CNR.

Conclusions: Four-tissue class AC may impact SUV and K_i parameter estimation but only to a limited extent, thereby suggesting that WB Patlak K_i imaging for dynamic WB PET/MRI studies is feasible. Patlak K_i imaging can enhance TBR, thereby facilitating lesion segmentation and quantification. However, patient-specific A_{coeff} for each tissue class should be used when possible to address the high inter-patient variability of A_{coeff} distributions.

Key words: Whole-body PET/MRI, SUV, Patlak analysis, Tissue classification, Attenuation correction

Introduction

Positron emission tomography/magnetic resonance imaging (PET/MRI) is a two-in-one hybrid imaging technology that could provide competitive advantages over PET/X-ray computed tomography (PET/CT), including superior soft tissue contrast, advanced options for multiparametric MRI and MR spectroscopy, superior motion-tracking capabilities, and reduced radiation exposure [1]. A number of studies reported that 2-deoxy-2-[18F]fluoro-D-glucose ([18F]FDG) PET/MRI has the potential to qualitatively and quantitatively improve tumor characterization in breast cancer [2, 3]. Xin et al. [4] also reported that PET/MRI could provide good image quality suitable for the detection of abdominal and pelvic tumors. Using PET/MRI, improved diagnostic performance in patients with colorectal cancer liver metastases was also observed, compared with PET or CT imaging [5]. Likewise, [18F]FDG-PET combined with diffusion-weighted MRI was reported to yield excellent results for detection and T-classification of squamous cell carcinoma of the head and neck after radio(chemo)therapy [6].

One of the challenges in whole-body (WB) PET/MRI is the lack of proper attenuation maps (μ-map) at 511-keV annihilation photons suitable for PET attenuation correction (AC) as the intensity of MR images depends on proton density and relaxation properties, which is not related to photon attenuation properties. A number of AC strategies in WB PET/MRI have been proposed during the last decade [7]. These methods could be roughly divided into segmentation-based [8, 9], template/atlas-based [10, 11], and reconstruction-based approaches [12, 13]. Previous studies have shown that segmentation-based methods could be a potentially reliable AC approach for WB PET/MRI, as they result in acceptable quantitative standardized uptake value (SUV) images [8]. However, a number of other studies indicated substantial quantitative bias particularly when considering tracer uptake at the regional level and in proximity to bony structures [14–16].

The SUV is extensively used as an index to assess the activity of a wide range of molecular processes associated with cancer cells. However, conventional SUV PET imaging only presents the three-dimensional (3D) spatial distribution of a tracer's activity concentration averaged over a single time frame of a PET acquisition. Recently, there has been increasing interest in dynamic WB Patlak-derived net uptake rate constant (K_i) PET imaging owing to its ability to estimate K_i parametric images across the whole human body as a complement to standard-of-care SUV imaging [17–23]. Unlike static acquisitions and the SUV metric, dynamic PET imaging allows for tracking of the four-dimensional (4D) spatio-temporal distribution of the tracer uptake post-injection, thereby enabling the estimation of the tracer's K_i value which may be of high clinical importance for certain types of malignancy.

Our previous studies reported on a clinically feasible WB dynamic PET acquisition protocol using both indirect and direct 4D Patlak reconstruction methods [17–23]. The purpose of the present study is to investigate the impact of four-tissue class segmentation in MRI-guided attenuation correction of SUV and Patlak K_i images to assess the feasibility of WB Patlak PET/MRI. It would be important to demonstrate the potential adoption of WB parametric imaging to clinical oncological PET/MRI studies to further benefit from the competitive advantages of multiparametric capabilities of MRI.

Materials and Methods

Patient Population

WB dynamic PET data were collected from 14 patients enrolled from 2014 to 2017. All patients underwent WB [18F]FDG PET/CT scans at Geneva university Hospital. Patient characteristics are shown in Suppl. Table S1, see Electronic Supplementary Material (ESM). The study was approved by the local ethics committee.

Whole-Body PET/CT Acquisition Protocol

A previously proposed clinical WB dynamic PET acquisition protocol [17, 18, 21, 23, 24] was adapted for the Siemens Biograph mCT Flow™ scanner. The scan protocol included an initial dynamic PET cardiac scan (12×10 s and 12×20 s frames) over a single bed position during the first 6 min post-injection (1st phase), followed by 13 WB passes acquired with continuous bed motion (CBM) mode (2nd phase), each lasting 3 min. Conventional static SUV PET images were subsequently acquired in CBM mode over the same WB field-of-view. All list-mode raw PET data from WB dynamic and static scans, along with the low-dose CT images, were archived for later offline data processing.

Tissue Classification for Derivation of MRI-Guided Attenuation Maps

The μ-map from the corresponding CT images was generated using the bilinear transformation technique (μ-map$_{CTAC}$) [25]. Subsequently, the segmented μ-map with four-tissue classes (μ-map$_{4\text{-classes}}$) was obtained to represent typical μ-map generated for AC on PET/MRI systems. We considered four-tissue classes, namely background (air), lung, fat, and soft tissue, according to the tissue classification technique proposed by Martinez-Möller et al. [8]. Specifically, the voxels with attenuation coefficient (A_{coeff}) values not larger than 0.005 cm^{-1} in μ-map$_{CTAC}$ were defined as background and assigned a predefined A_{coeff} value of 0 cm^{-1}, voxels above 0.005 cm^{-1} and not larger than 0.05 cm^{-1} were classified as lung with an A_{coeff} value of 0.018 cm^{-1}, voxels in the range of 0.05 cm^{-1} and 0.093 cm^{-1} were considered as fat (0.086 cm^{-1}), and voxels above 0.093 cm^{-1} were defined as soft tissue and assigned an A_{coeff} value of 0.10 cm^{-1}. To assess the influence of bones in AC, the respective μ-map without bones (μ-map$_{no\text{-bones}}$) was also generated by substituting the voxels having A_{coeff} over 0.105 cm^{-1} (identified as bones) with the value of 0.1 cm^{-1} (soft tissue) in μ-map$_{CTAC}$. The flowchart of the three different AC methods is summarized in Suppl. Fig. S1 (see ESM).

Reconstruction of Conventional SUV PET Images

Using the e7tool PET reconstruction software (Siemens Healthcare, Knoxville, TN), all acquired list-mode raw PET data was converted into sinograms and later reconstructed using μ-map$_{CTAC}$, μ-map$_{4\text{-classes}}$, and μ-map$_{no\text{-bones}}$ to generate PET SUV images (PET$_{CTAC}$, PET$_{4\text{-classes}}$, and PET$_{no\text{-bones}}$), respectively. The ordinary Poisson ordered subsets expectation maximization (OP-OSEM) with 2 iterations and 21 subsets, including point spread function (PSF) and time-of-flight (TOF), was adopted for the reconstruction. The reconstruction matrix for the first 24 cardiac PET frames was $400 \times 400 \times 109$ with a voxel

size of $2.036 \times 2.036 \times 2.027$ mm^3, while for the last 13 WB passes, the matrix size was $200 \times 200 \times 109$ with a voxel size of $4.073 \times 4.073 \times 2.027$ mm^3. All dynamic PET images were subsequently smoothed using a standard Gaussian filter of 2 mm full-width at half-maximum.

Input Function Derivation

The input function, which is defined as the time course of the tracer's activity concentration in the blood plasma, is required to estimate the Patlak parameters. In our study, the input function was derived with in-house developed computer program from all 37 (24 + 13) dynamic cardiac PET frames by extracting the activity from a region-of-interest (ROI) carefully drawn in the center of the heart's left ventricle as distant as possible from the myocardium wall to minimize any partial volume effects.

Whole-Body PET Patlak Analysis

In this study, we estimated the Patlak parameters of K_i and total blood distribution volume (V) at the voxel level to enable WB parametric imaging. For that purpose, the time course of the tissue activity concentration at every voxel, also known as voxel time–activity curve (TAC), was extracted. Subsequently, the input function and the TAC at each voxel were fitted to the Patlak analysis model to estimate the respective K_i and V parameters using the ordinary least squares (OLS) Patlak regression method. The Patlak regression method can be conducted post-reconstruction to indirectly estimate K_i and V images from the dynamic images [17, 18]. Alternatively, Patlak modeling can be incorporated within the system matrix of the OP-OSEM algorithm to directly reconstruct the K_i and V images [26, 27]. For indirect parametric reconstruction, 13 PET sinograms were independently reconstructed using the same reconstruction protocol as for SUV images. Then, OLS Patlak post-reconstruction regression was then applied on the 13 dynamic PET images to generate indirect WB parametric K_i images. For direct parametric reconstruction, the Patlak parametric reconstruction was performed on 13 PET sinograms directly to estimate WB K_i images. In-house developed computer code was used for both indirect and direct parametric reconstruction processing.

PET Image Analysis

To delineate the metabolically active tumor volume (MATV) for the lesions in smoothed PET images, a method for automatic segmentation using an active contour model (MASAC) was employed [28]. The algorithm has previously been validated for accuracy and robustness using phantom and clinical studies. Quantitative metrics including MATV,

peak value in ROI (ROI$_{peak}$), maximum value in ROI (ROI$_{max}$), mean value in ROI (ROI$_{mean}$), and metabolic volume product (MVP) were extracted from the same regions in SUV and respective K_i images. Specifically, the MVP is defined as follows:

$$MVP = MATV \times ROI_{mean} \qquad (1)$$

The MVP calculated from ROI$_{mean}$ measurements of SUV images is also known as total lesion glycolysis (TLG), while the respective metric for K_i images is known as metabolic rate volume (MRV) [29].

To assess the contrast and noise in images, the target-to-background (TBR) and contrast-to-noise ratio (CNR) metrics were adopted. They are defined as follows:

$$TBR = \frac{Mean_T}{Mean_B} \qquad (2)$$

$$CNR = \frac{Mean_T - Mean_B}{Std_B} \qquad (3)$$

where Mean$_T$ and Mean$_B$ are the mean tracer uptake in the target (tumor) and background regions, respectively. Std$_B$ is the standard deviation in the background region.

The relative difference (RE) of quantitative metrics derived from PET$_{4\text{-classes}}$ and PET$_{no\text{-bones}}$ with respect to PET$_{CTAC}$ (RE$_{4\text{-classes}}$/RE$_{no\text{-bones}}$) is defined as follows:

$$RE_{4-classes} = \frac{PET_{4-classes} - PET_{CTAC}}{PET_{CTAC}} \times 100\% \qquad (4)$$

$$RE_{no-bones} = \frac{PET_{no-bones} - PET_{CTAC}}{PET_{CTAC}} \times 100\% \qquad (5)$$

Statistical Analysis

Statistical analysis was performed using IBM SPSS Statistics 24.0 software (IBM, Chicago, USA). The non-parametric Wilcoxon test was conducted to assess the difference between PET$_{4\text{-classes}}$ and PET$_{no\text{-bones}}$ against PET$_{CTAC}$. The same test was also adopted to compare the difference between SUV and indirect K_i, SUV and direct K_i, or indirect K_i and direct K_i. A P value < 0.05 was considered to be significant. In addition, the non-parametric Spearman correlation analysis was performed to assess the potential relationships between PET$_{CTAC}$ and PET$_{4\text{-classes}}$ as well as between PET$_{CTAC}$ and PET$_{no\text{-bones}}$.

Results

Comparisons Between PET$_{4\text{-classes}}$ and PET$_{CTAC}$

Representative slices from μ-map$_{CTAC}$, μ-map$_{4\text{-classes}}$, and μ-map$_{no\text{-bones}}$ are shown in Fig. 1. Slices depicting the difference between PET$_{4\text{-classes}}$ and PET$_{CTAC}$ for SUV, indirect K_i, and direct K_i images are presented in Fig. 2. A slightly higher difference could be observed for SUV images, compared with K_i images.

As shown in Table 1, no significant difference in MATV, TBR, and CNR could be observed between PET$_{4\text{-classes}}$ and PET$_{CTAC}$ for all patients, either for SUV or K_i images. To the contrary, PET$_{4\text{-classes}}$ significantly overestimated ROI$_{peak}$, ROI$_{max}$, ROI$_{mean}$, as well as the MVP scores compared to PET$_{CTAC}$. Detailed quantitative analysis showed that SUV images achieved the highest median RE$_{4\text{-classes}}$ with 6.91 %, 6.55 %, 5.90 %, and 6.56 % for ROI$_{peak}$, ROI$_{max}$, ROI$_{mean}$, and MVP, whereas K_i images showed slightly reduced RE$_{4\text{-classes}}$ (indirect 5.52 %, 5.95 %, 4.43 %, and 5.70 %, direct 6.61 %, 6.33 %, 5.53 %, and 4.96 %) for ROI$_{peak}$, ROI$_{max}$, ROI$_{mean}$, and MVP, respectively. The RE$_{4\text{-classes}}$ for most metrics did not show any significant difference between SUV and indirect K_i, SUV and direct K_i, or indirect K_i and direct K_i PET images. The only exception was observed for RE$_{4\text{-classes}}$ for ROI$_{peak}$ between SUV and indirect K_i images (Fig. 3). Metrics derived from PET$_{4\text{-classes}}$ were highly correlated with those
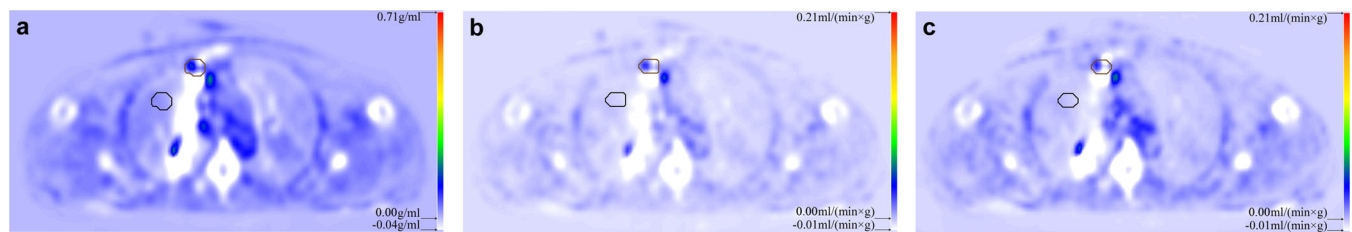

Fig. 1. **a** Representative slices in the thorax region showing μ-map$_{CTAC}$. **b** μ-map$_{4\text{-classes}}$. **c** μ-map$_{no\text{-bones}}$.

Fig. 2. Representative slice of a clinical study showing the difference images between PET_{CTAC} and $PET_{4\text{-classes}}$ ($PET_{4\text{-classes}}$ − PET_{CTAC}) for **a** SUV, **b** indirect K_i, and **c** direct K_i images. The contours defined by the MASAC algorithm (brown) and background regions (black) on $PET_{4\text{-classes}}$ images are also shown. Note that different scales were used for SUV and K_i images.

from PET_{CTAC} ($P < 0.001$, correlation coefficients > 0.98) for all images. A similar trend could also be observed for the lung data, as depicted in Table 2.

Comparisons of SUV, Indirect K_i, and Direct K_i PET Images

Figure 4 shows representative segmentation results for SUV, indirect K_i, and direct K_i $PET_{4\text{-classes}}$ images. One can observe that both indirect and direct K_i $PET_{4\text{-classes}}$ images achieve higher TBR compared with SUV $PET_{4\text{-classes}}$ images. The MASAC segmentation algorithm could properly delineate the lesion on all images. Another representative clinical study is shown in Suppl. Fig. S2 (see ESM).

For all clinical studies, indirect K_i $PET_{4\text{-classes}}$ images exhibited the lowest values in MATV (5.14 cm^3) whereas no significant difference in MATV could be observed between SUV and direct K_i $PET_{4\text{-classes}}$ images (Fig. 5). Both indirect and direct K_i $PET_{4\text{-classes}}$ images provided higher TBR (indirect 11.3, direct 10.4) than SUV $PET_{4\text{-classes}}$ images (3.4). Although no significant difference could be established in CNR between SUV and indirect K_i $PET_{4\text{-classes}}$ images, direct K_i $PET_{4\text{-classes}}$ images showed higher CNR (30.6) compared with indirect K_i (19.0) and SUV (21.4) $PET_{4\text{-classes}}$ images, respectively. Similar results were observed for the lung data (Fig. 5). A similar trend was also observed in the comparisons between SUV, indirect K_i, and direct K_i PET_{CTAC} and $PET_{no\text{-bones}}$ images.

Influence of Bone in MRI-Guided AC

When bony structures are classified as soft tissue and assigned a predefined A_{coeff} of 0.1 cm^{-1}, no statistically significant differences were observed in MATV, TBR, and CNR scores relative to PET_{CTAC}, except for MATV in indirect K_i images (Table 3). However, the ROI_{peak}, ROI_{max}, ROI_{mean}, as well as the MVP scores were underestimated by 1 % ($P < 0.05$) for all clinical studies in most comparisons, except for MVP in direct K_i images. Similar results were also obtained for the lung data (Table 4).

Discussion

Our previous studies have proposed and validated a WB dynamic PET acquisition protocol for routine clinical imaging [17–23]. It is feasible to combine SUV and Patlak K_i WB PET imaging in clinical oncology within a single clinical acceptable scanning time [30]. This newly developed parametric K_i PET imaging framework, when applied for WB PET/MRI studies, might offer a more integrated solution for cancer imaging at a lower cost and with the competitive advantages of MRI. Different MRI-guided AC methods have been extensively assessed on SUV images using either simulation or clinical studies. In this work, we observed that the four-tissue class segmentation for MRI-guided AC may be applied to WB Patlak PET/MRI without affecting K_i quantification to a large extent, thereby suggesting that parametric K_i imaging in WB PET/MRI is feasible in clinical setting. Although AC with μ-map$_{4\text{-classes}}$ had no statistically significant impact on MATV

Table 1. Relative difference of quantitative metrics derived from $PET_{4\text{-classes}}$ with respect to PET_{CTAC} ($\frac{PET_{4\text{-classes}} - PET_{CTAC}}{PET_{CTAC}} \times 100\%$, $RE_{4\text{-classes}}$) for SUV, indirect K_i and direct K_i images for all patient data. Data are presented as median [inter-quartile range], with $P < 0.05$ (Wilcoxon test between $PET_{4\text{-classes}}$ and PET_{CTAC}) marked by asterisk

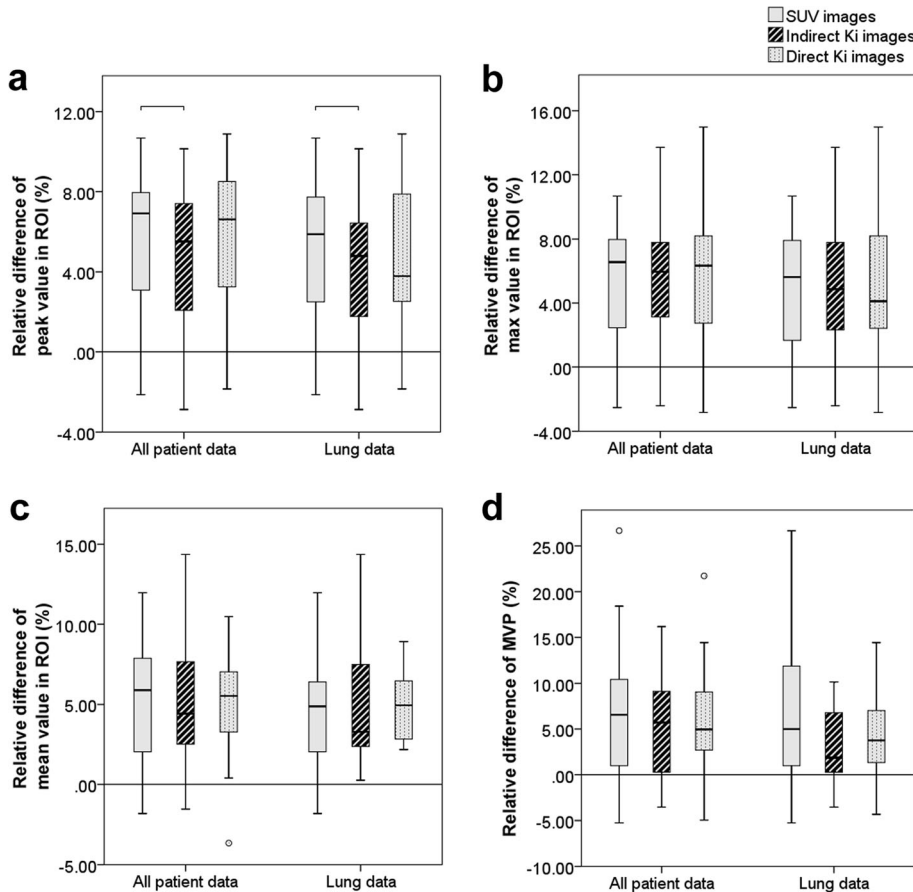|	SUV images	Indirect K_i images	Direct K_i images
MATV (%)	0.28 [−2.30, 3.93]	0.00 [−1.46, 2.65]	−0.22 [−2.55, 2.39]
TBR (%)	1.09 [−0.53, 5.40]	−0.09 [−3.82, 7.33]	0.10 [−5.71,9.07]
CNR (%)	2.75 [−3.44, 7.84]	−0.21 [−4.18, 5.77]	−0.57 [−7.47, 7.65]
ROI_{peak} (%)	6.91 [2.94, 8.01]*	5.52 [2.00, 7.63]*	6.61 [3.07, 8.52]*
ROI_{max} (%)	6.55 [2.26, 7.98]*	5.95 [2.93, 7.83]*	6.33 [2.66, 8.27]*
ROI_{mean} (%)	5.90 [1.71, 7.97]*	4.43 [2.48, 7.68]*	5.53 [3.17, 7.24]*
MVP (%)	6.56 [0.79, 10.71]*	5.70 [0.26, 9.20]*	4.96 [2.35, 9.13]*

Fig. 3. Relative difference in **a** peak, **b** max, and **c** mean values in region-of-interest (ROI) and **d** metabolic volume product (MVP) derived from PET$_{4\text{-classes}}$ with respect to PET$_{CTAC}$ ($\frac{\text{PET}_{4\text{-classes}} - \text{PET}_{CTAC}}{\text{PET}_{CTAC}} \times 100\%$) with all patient studies and lung data. Outliers identified as 1.5× inter-quartile range. Comparisons with statistically significant differences (Wilcoxon test) are marked with a horizontal line.

segmentation, TBR, and CNR, compared to AC with μ-map$_{CTAC}$, on either SUV or K_i images, μ-map$_{4\text{-classes}}$ demonstrated a limited but non-negligible effect on SUV and K_i estimation. Moreover, the enhanced TBR of K_i images over SUV indicated that WB K_i imaging may facilitate lesion segmentation and quantification in PET/MRI when applied as a complement to SUV imaging.

Our quantitative assessment revealed an overestimation of SUV and K_i when performing AC using μ-map$_{4\text{-classes}}$.

This finding initially appears to be inconsistent with the results of Martinez-Möller et al. [8], who reported that SUV is underestimated on average in the lung lesions by 2 %. Nevertheless, this discrepancy can be explained by the difference between the actual attenuation coefficients in lung lesions and the predefined A_{coeff} assigned to the lung class. Indeed, most of the lesions in our study were found to be assigned higher attenuation coefficients in μ-map$_{4\text{-classes}}$ compared with the actual A_{coeff} derived from μ-map$_{CTAC}$,

Table 2. RE$_{4\text{-classes}}$ of quantitative metrics for SUV, indirect K_i, and direct K_i images for the lung data. Data are presented as median [inter-quartile range], with $P < 0.05$ (Wilcoxon test between PET$_{4\text{-classes}}$ and PET$_{CTAC}$) marked by asterisk

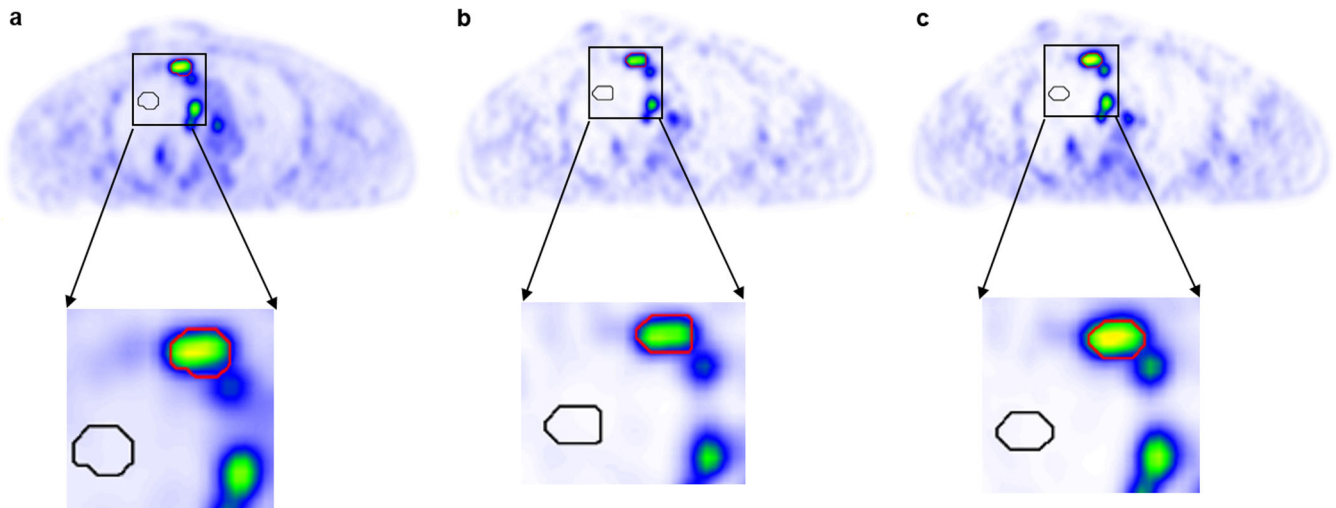|	SUV images	Indirect K_i images	Direct K_i images
MATV (%)	1.65 [−3.50, 7.94]	−0.90 [−3.36, 1.32]	−0.71 [−4.86, 2.44]
TBR (%)	2.59 [−1.69, 8.54]	−0.11 [−4.96, 9.77]	2.46 [−5.85, 9.85]
CNR (%)	5.43 [−1.56, 15.01]	2.24 [−4.93, 10.07]	−0.77 [−9.62, 12.22]
ROI$_{peak}$ (%)	5.88 [1.67, 8.33]*	4.80 [1.57, 7.88]*	3.79 [2.16, 8.19]*
ROI$_{max}$ (%)	5.62 [1.18, 8.57]*	4.87 [1.86, 8.93]*	4.12 [2.02, 8.42]*
ROI$_{mean}$ (%)	4.88 [1.37, 6.93]*	3.29 [1.92, 8.30]*	4.95 [2.64, 6.67]*
MVP (%)	4.99 [0.39, 14.14]*	1.85 [−0.31, 7.95]*	3.76 [0.59, 7.13]*

Fig. 4. Representative slices of a clinical study showing **a** SUV, **b** indirect K_i, and **c** direct K_i PET$_{4\text{-classes}}$ images showing contours for the segmentation results (red) and background regions (black) on the respective images.

which naturally led to overestimation of correction factors, which in turn, resulted in higher SUV and K_i values in PET$_{4\text{-classes}}$ [31].

The median RE$_{4\text{-classes}}$ of K_i is slightly smaller in parametric K_i images than in SUV images, although the RE$_{4\text{-classes}}$ for most metrics did not show any significant difference between SUV and indirect K_i, SUV and direct K_i, or indirect K_i and direct K_i PET images. The only exception was observed for RE$_{4\text{-classes}}$ in ROI$_{peak}$ between SUV and K_i images. The findings of previous studies have also shown that parametric K_i images presented slightly reduced bias with respect to four-tissue class AC, compared to the respective bias presented in SUV images [32].

In our study, a higher TBR was observed in both indirect and direct K_i images compared to the SUV images, which may improve the lesion detectability in the clinic [23]. It

should be noted that although no significant differences could be established in CNR between SUV and indirect K_i images, direct K_i images significantly improved CNR compared with indirect K_i and SUV images. Our results are consistent with previous studies who reported superior CNR in direct K_i images compared with indirect K_i and SUV images owing to the noise reduction observed in direct *vs.* indirect K_i images and the superior contrast observed in indirect and direct K_i against SUV images [19]. Our recent work using a dynamic phantom simulation framework also demonstrated enhanced TBR in indirect K_i images compared with SUV images [21].

The lung tissue is expected to exercise the largest impact on SUV estimates because of its large volume. Moreover, the high inter-patient variability observed in the actual A_{coeff} distribution within the lungs is expected to lead to
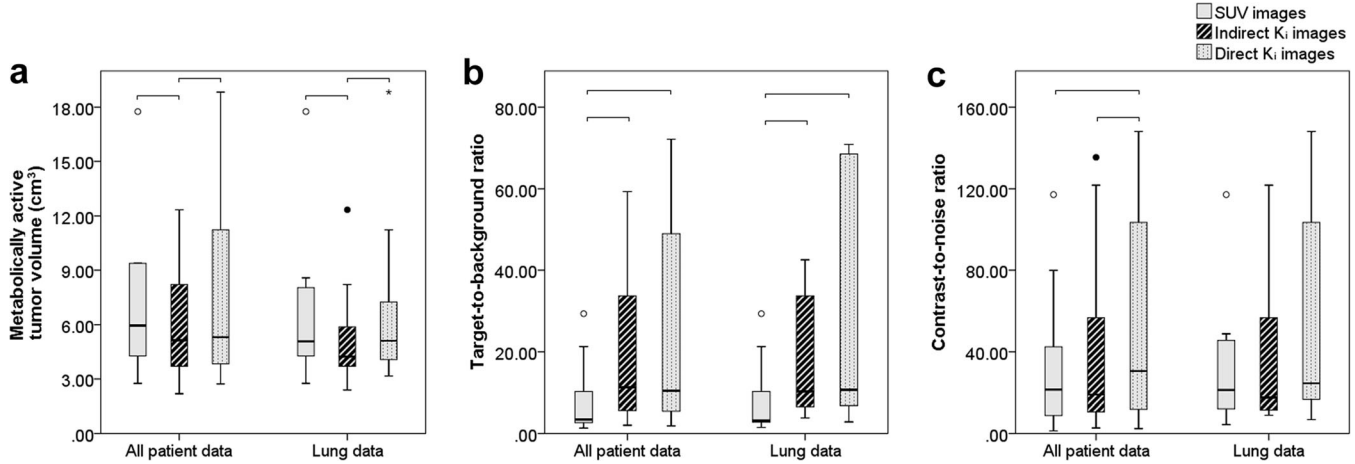

Fig. 5. Box and whisker plots representing **a** metabolically active tumor volume, **b** target-to-background ratio, and **c** contrast-to-noise ratio for SUV, indirect K_i, and direct K_i PET$_{4\text{-classes}}$ images for clinical studies and lung data. Outliers identified as 1.5× inter-quartile range. Comparisons with statistically significant differences (Wilcoxon test) are marked with a horizontal line.

Table 3. Relative difference of quantitative metrics derived from $PET_{no-bones}$ with respect to PET_{CTAC} ($\frac{PET_{no-bones}-PET_{CTAC}}{PET_{CTAC}} \times 100\%$, $RE_{no-bones}$) for SUV, indirect K_i, and direct K_i images for all clinical studies. Data are presented as median [inter-quartile range], with $P < 0.05$ (Wilcoxon test between $PET_{no-bones}$ and PET_{CTAC}) marked by asterisk

	SUV images	Indirect K_i images	Direct K_i images
MATV (%)	0.00 [−0.63, 0.84]	0.00 [0.00, 0.57]*	0.00 [−0.57, 1.48]
TBR (%)	−0.17 [−1.21, 0.51]	−0.33 [−2.55, 0.87]	−0.32 [−2.95, 1.79]
CNR (%)	−0.34 [−1.43, 0.86]	−0.81 [−2.35, 0.41]	−0.38 [−3.06, 0.86]
ROI_{peak} (%)	−1.21 [−1.78, −0.78]*	−1.12 [−1.84, −0.77]*	−1.05 [−1.43, −0.81]*
ROI_{max} (%)	−1.31 [−1.87, −0.84]*	−1.18 [−1.94, −0.84]*	−1.14 [−1.48, −0.73]*
ROI_{mean} (%)	−1.03 [−1.90, −0.71]*	−1.31 [−2.02, −0.81]*	−1.18 [−1.85, −0.54]*
MVP (%)	−1.07 [−1.76, −0.62]*	−1.03 [−1.35, −0.70]*	−1.03 [−1.39, 0.54]

considerable bias in quantitative PET/MRI if a predefined A_{coeff} is assigned to μ-map$_{4-classes}$ for all patients. Indeed, as reported by Keereman et al. [14], more than 10 % inter-patient variability could be observed in lung A_{coeff}. The lung density is significantly different from one patient to another, depends on breathing patterns, and varies with age and in the event of respiratory diseases by as much as 30 % [33]. This issue should be carefully considered in quantitative analysis of PET/MRI results.

Therefore, it is recommended that customized A_{coeff} are provided for each tissue class of the segmented μ-map$_{4-classes}$ for each patient when possible. More specifically, patient-specific A_{coeff} may be derived for some tissue classes when CT-based anatomical data are retrospectively available for a given patient. For instance, radiation therapy patients commonly undergo a CT simulation study on a dedicated X-ray simulator and/or verify the accuracy of positioning using cone beam CT. Hence, it would be meaningful to exploit those images for the derivation of personalized attenuation coefficients for each tissue. The feasibility of utilizing MRI in dose calculation without CT images in radiation therapy has also been demonstrated in recent years [34, 35].

Currently, two variants of segmentation methods for tissue classification have been implemented on commercial PET/MRI systems, namely the three-class μ-map (air, lung and soft tissue) [36] and four-class μ-map (air, lung, fat, and soft tissue) [8]. In this work, we focused particularly on the latter AC method, which can be derived using the 2-point Dixon MRI sequence, because it has been substantiated that the four-tissue class segmentation can achieve higher accuracy in AC of PET/MRI studies compared with the three-class AC approach [15]. It should also be noted that

bones are not segmented in μ-map$_{4-classes}$ because it remains challenging to correctly identify all types of bone tissues from conventional MRI sequences. Previous studies have shown that the five-tissue class (cortical bone, spongeous bone, soft tissue, lung, and air) approach improves the accuracy of MRI-guided AC compared to four-tissue class (cortical bone, soft tissue, lung, and air) segmentation [14, 15].

Our study has shown that the bone removal from μ-map caused an underestimation of bone AC, leading to a decrease (1 %) in SUV and K_i estimation compared to AC using μ-map$_{CTAC}$. Recent studies have shown that the accuracy of MRI-guided AC could be substantially improved in PET/MRI when considering bones, especially for the diagnosis and assessment of treatment response of cancer patients with bone metastases [9, 15]. Cortical bone discrimination is required for AC in PET/MRI, although cortical bone does not occupy a large volume within the body [14]. Berker et al. [37] demonstrated the feasibility of utilizing ultrashort-echo-time (UTE) MR sequences in the clinic for tissue classification into four classes (air, adipose, soft, and bone tissues) in PET/MRI. However, bone tissues exhibit high inter-patient variability and the lung tissue is not classified in that method. Fast zero-echo-time (ZTE) MR imaging was also proposed as an alternative approach; however, the acquisition time remain very long, which limits the applicability of this technique in WB PET/MRI [38].

In our study, we included in our analysis the ROI_{peak} metric for SUV and K_i images. The ROI_{peak} metric has been recently recommended as a more robust alternative to ROI_{max} [39]. The ROI_{max} and ROI_{mean} metrics are widely adopted for the assessment of different AC methods in PET/MRI. However, ROI_{max} can be highly sensitive to statistical

Table 4. $RE_{no-bones}$ of quantitative metrics for SUV, indirect K_i and direct K_i images for the lung data. Data are presented as median [inter-quartile range], with $P < 0.05$ (Wilcoxon test between $PET_{no-bones}$ and PET_{CTAC}) marked by asterisk

	SUV images	Indirect K_i images	Direct K_i images
MATV (%)	0.00 [−0.69, 0.94]	0.00 [0.00, 0.28]	0.00 [−1.05, 0.60]
TBR (%)	0.00 [−0.74, 0.53]	−0.98 [−2.84, 0.75]	−0.39 [−2.79, 1.71]
CNR (%)	−0.26 [−0.76, 2.01]	−1.11 [−2.44, −0.20]	−1.10 [−3.39, 1.23]
ROI_{peak} (%)	−1.13 [−1.49, −0.73]*	−0.98 [−1.58, −0.70]*	−1.15 [−1.56, −0.16]*
ROI_{max} (%)	−1.08 [−1.53, −0.71]*	−0.96 [−1.59, −0.68]*	−1.01 [−1.36, −0.39]*
ROI_{mean} (%)	−0.95 [−1.69, −0.47]*	−1.11 [−2.21, −0.78]*	−0.99 [−2.03, −0.20]*
MVP (%)	−1.03 [−1.28, −0.64]*	−0.96 [−1.35, −0.75]*	−1.27 [−1.95, 0.07]*

noise present in PET images as it only reflects the activity of a single voxel. Conversely, ROI$_{mean}$ metric is highly sensitive to partial volume effect and is significantly affected by the MATV definition.

Further discussion of our findings and the limitations of this study are given in the ESM.

Conclusions

This work demonstrated that the four-tissue class segmentation in MRI-guided AC may impact WB Patlak PET/MRI, but only to a limited extent, thereby suggesting that parametric K_i imaging in WB PET/MRI is feasible in clinical setting. Compared to AC using μ-map$_{CTAC}$, we did not observe any statistically significant impact on MATV, TBR, and CNR when using μ-map$_{4\text{-classes}}$ for AC. However, a small but non-negligible effect on SUV and K_i scores was observed. Moreover, Patlak K_i imaging led to enhanced TBR, regardless of the AC method, thereby indicating that WB Patlak PET/MRI may facilitate lesion segmentation and quantification when complementing standard-of-care SUV imaging. Finally, it is important to consider, whenever possible, patient-specific attenuation coefficients for each tissue class of the MRI-guided AC maps to address any mismatch with actual attenuation coefficients distribution, due to their high inter-patient variability.

Compliance with Ethical Standards

The study was approved by the local ethics committee.

Conflict of Interest

The authors declare that they have no conflict of interest.

Publisher's Note. Springer Nature remains neutral with regard to jurisdictional claims in published maps and institutional affiliations.

References

1. Zaidi H, Becker M (2016) The promise of hybrid PET/MRI: technical advances and clinical applications. IEEE Sign Proc Mag 33:67–85

2. Cho N, Im SA, Cheon GJ, Park IA, Lee KH, Kim TY, Kim YS, Kwon BR, Lee JM, Suh HY, Suh KJ (2018) Integrated ^{18}F-FDG PET/MRI in breast cancer: early prediction of response to neoadjuvant chemotherapy. Eur J Nucl Med Mol Imaging 45:328–339

3. Plecha DM, Faulhaber P (2017) PET/MRI of the breast. Eur J Radiol 94:A26–A34

4. Xin J, Ma Q, Guo Q, Sun H, Zhang S, Liu C, Zhai W (2016) PET/MRI with diagnostic MR sequences vs PET/CT in the detection of abdominal and pelvic cancer. Eur J Radiol 85:751–759

5. Lee DH, Lee JM, Hur BY, Joo I, Yi NJ, Suh KS, Kang KW, Han JK (2016) Colorectal cancer liver metastases: diagnostic performance and prognostic value of PET/MR imaging. Radiology 280:782–792

6. Becker M, Varoquaux AD, Combescure C, Rager O, Pusztaszeri M, Burkhardt K, Delattre BMA, Dulguerov P, Dulguerov N, Katirtzidou E, Caparrotti F, Ratib O, Zaidi H, Becker CD (2018) Local recurrence of squamous cell carcinoma of the head and neck after radio(chemo)-therapy: diagnostic performance of FDG-PET/MRI with diffusion-weighted sequences. Eur Radiol 28:651–663

7. Mehranian A, Arabi H, Zaidi H (2016) Vision 20/20: magnetic resonance imaging-guided attenuation correction in PET/MRI: challenges, solutions, and opportunities. Med Phys 43:1130–1155

8. Martinez-Möller A, Souvatzoglou M, Delso G et al (2009) Tissue classification as a potential approach for attenuation correction in whole-body PET/MRI: evaluation with PET/CT data. J Nucl Med 50:520–526

9. Kim JH, Lee JS, Song IC, Lee DS (2012) Comparison of segmentation-based attenuation correction methods for PET/MRI: evaluation of bone and liver standardized uptake value with oncologic PET/CT data. J Nucl Med 53:1878–1882

10. Arabi H, Zaidi H (2016) Magnetic resonance imaging-guided attenuation correction in whole-body PET/MRI using a sorted atlas approach. Med Image Anal 31:1–15

11. Burgos N, Cardoso MJ, Thielemans K, Modat M, Dickson J, Schott JM, Atkinson D, Arridge SR, Hutton BF, Ourselin S (2015) Multi-contrast attenuation map synthesis for PET/MR scanners: assessment on FDG and Florbetapir PET tracers. Eur J Nucl Med Mol Imaging 42:1447–1458

12. Mehranian A, Zaidi H (2015) Joint estimation of activity and attenuation in whole-body TOF PET/MRI using constrained Gaussian mixture models. IEEE Trans Med Imaging 34:1808–1821

13. Rezaei A, Deroose CM, Vahle T, Boada F, Nuyts J (2018) Joint reconstruction of activity and attenuation in time-of-flight PET: a quantitative analysis. J Nucl Med 59:1624–1629

14. Keereman V, Van Holen R, Mollet P, Vandenberghe S (2011) The effect of errors in segmented attenuation maps on PET quantification. Med Phys 38:6010–6019

15. Akbarzadeh A, Ay MR, Ahmadian A, Alam NR, Zaidi H (2013) MRI-guided attenuation correction in whole-body PET/MR: assessment of the effect of bone attenuation. Ann Nucl Med 27:152–162

16. Arabi H, Rager O, Alem A, Varoquaux A, Becker M, Zaidi H (2015) Clinical assessment of MR-guided 3-class and 4-class attenuation correction in PET/MR. Mol Imaging Biol 17:1–13

17. Karakatsanis NA, Lodge MA, Tahari AK, Zhou Y, Wahl RL, Rahmim A (2013) Dynamic whole-body PET parametric imaging: I. Concept, acquisition protocol optimization and clinical application. Phys Med Biol 58:7391–7418

18. Karakatsanis NA, Lodge MA, Zhou Y, Wahl RL, Rahmim A (2013) Dynamic whole-body PET parametric imaging: II. Task-oriented statistical estimation. Phys Med Biol 58:7419–7445

19. Karakatsanis NA, Casey ME, Lodge MA, Rahmim A, Zaidi H (2016) Whole-body direct 4D parametric PET imaging employing nested generalized Patlak expectation-maximization reconstruction. Phys Med Biol 61:5456–5485

20. Zaidi H, Karakatsanis N (2018) Towards enhanced PET quantification in clinical oncology. Br J Radiol 91:20170508

21. Zhuang M, Karakatsanis NA, Dierckx R, Zaidi H (2019) Quantitative analysis of heterogeneous ^{18}F-FDG static (SUV) vs. Patlak (Ki) whole-body PET imaging using different segmentation methods: a simulation study. Mol Imaging Biol. https://doi.org/10.1007/s11307-018-1241-8

22. Rahmim A, Lodge MA, Karakatsanis NA et al (2019) Dynamic whole-body PET imaging: principles, potentials and applications. Eur J Nucl Med Mol Imaging. https://doi.org/10.1007/s00259-018-4153-6

23. Fahrni G, Karakatsanis N, Di Domenicantonio G, Garibotto V, Zaidi H (2019) Does whole-body Patlak ^{18}F-FDG PET imaging improve lesion detectability in clinical oncology? Eur Radiol https://doi.org/10.1007/s00330-018-5966-1

24. Karakatsanis NA, Zhou Y, Lodge MA, Casey ME, Wahl RL, Zaidi H, Rahmim A (2015) Generalized whole-body Patlak parametric imaging for enhanced quantification in clinical PET. Phys Med Biol 60:8643–8673

25. Carney JP, Townsend DW, Rappoport V, Bendriem B (2006) Method for transforming CT images for attenuation correction in PET/CT imaging. Med Phys 33:976–983

26. Tsoumpas C, Thielemans K (2009) Direct parametric reconstruction from dynamic projection data in emission tomography including prior estimation of the blood volume component. Nucl Med Commun 30:490–493

27. Karakatsanis NA, Mehranian A, Casey ME, Zaidi H (2016) Direct 4D slice-wise whole-body parametric PET image reconstruction for continuous bed motion acquisitions. IEEE Nuclear Science Symposium & Medical Imaging Conference, Strasbourg, France, 29 October – 6 November 2016, pp 1–6

28. Zhuang M, Dierckx RA, Zaidi H (2016) Generic and robust method for automatic segmentation of PET images using an active contour model. Med Phys 43:4483–4494

29. Tixier F, Vriens D, Cheze-Le Rest C et al (2016) Comparison of tumor uptake heterogeneity characterization between static and parametric ^{18}F-FDG PET images in non-small cell lung cancer. J Nucl Med 57:1033–1039

30. Karakatsanis N, Lodge M, Fahrni G et al (2016) Simultaneous SUV/Patlak-4D whole-body PET: a multi-parametric 4D imaging framework for routine clinical application [abstract]. J Nucl Med 57:367

31. Ouyang J, Chun SY, Petibon Y, Bonab AA, Alpert N, El Fakhri G (2013) Bias atlases for segmentation-based PET attenuation correction using PET-CT and MR. IEEE Trans Nucl Sci 60:3373–3382

32. Karakatsanis N, Tsoumpas C, Zaidi H (2015) The impact of MR-guided PET attenuation correction on whole-body dynamic and parametric PET imaging [abstract]. J Nucl Med 56:1796

33. Robinson PJ, Kreel L (1979) Pulmonary tissue attenuation with computed tomography: comparison of inspiration and expiration scans. J Comput Assist Tomogr 3:740–748

34. Owrangi AM, Greer PB, Glide-Hurst CK (2018) MRI-only treatment planning: benefits and challenges. Phys Med Biol 63:05TR01

35. Arabi H, Dowling JA, Burgos N, Han X, Greer PB, Koutsouvelis N, Zaidi H (2018) Comparative study of algorithms for synthetic CT generation from MRI: consequences for MRI-guided radiation planning in the pelvic region. Med Phys 45:5218–5233

36. Schulz V, Torres-Espallardo I, Renisch S, Hu Z, Ojha N, Börnert P, Perkuhn M, Niendorf T, Schäfer WM, Brockmann H, Krohn T, Buhl A, Günther RW, Mottaghy FM, Krombach GA (2011) Automatic, three-segment, MR-based attenuation correction for whole-body PET/MR data. Eur J Nucl Med Mol Imaging 38:138–152

37. Berker Y, Franke J, Salomon A, Palmowski M, Donker HCW, Temur Y, Mottaghy FM, Kuhl C, Izquierdo-Garcia D, Fayad ZA, Kiessling F, Schulz V (2012) MRI-based attenuation correction for hybrid PET/MRI systems: a 4-class tissue segmentation technique using a combined ultrashort-echo-time/Dixon MRI sequence. J Nucl Med 53:796–804

38. Sekine T, Ter Voert EE, Warnock G et al (2016) Clinical evaluation of ZTE attenuation correction for brain FDG-PET/MR imaging-comparison with atlas attenuation correction. J Nucl Med 57:1927–1932

39. Avigaëlle S, Franck L, Pacôme F et al (2016) For avid glucose tumors, the SUV peak is the most reliable parameter for [18F]FDG-PET/CT quantification, regardless of acquisition time. EJNMMI Res 6:1–6